RESEARCH ARTICLE

Soret Influence in the Presence of Thermal Radiation, Heat Generation, and Chemical Reaction on Unsteady Magnetohydrodynamic Mixed Convective Oscillatory Flow through a Two-Phase Horizontal Channel

N. Avinash[1] **and Vediyappan Govindan**[2,*]

[1] Department of Mathematics, Sacred Heart College (Autonomous), Tirupattur 635 601, Tamil Nadu, India
[2] Department of Mathematics, Hindustan Institute of Technology and Science, Chennai, Tamil Nadu, India

Abstract

This paper analytically investigates unsteady, laminar, magnetohydrodynamic (MHD) mixed convective oscillatory flow of two immiscible viscous fluids through a horizontal two-phase channel. The channel consists of a porous upper region (Region I, $0 \leq y \leq h$) and a non-porous lower region (Region II, $-h \leq y \leq 0$), separated by a permeable interface, with a uniform transverse magnetic field B_0 applied normal to the flow. The governing equations incorporate thermal buoyancy (Gr), concentration buoyancy (Gc), Darcy porous resistance, thermal radiation (Rosseland approximation), volumetric heat generation/absorption, first-order destructive chemical reaction, and the Soret effect in both regions. An oscillatory suction/injection velocity is assumed at the walls, and a perturbation expansion in the small parameter $\varepsilon \ll 1$ decouples the system into zeroth-order (steady) and first-order (oscillatory) ODEs, solved analytically. Six interface conditions enforce continuity of velocity, shear stress, temperature, heat flux, concentration, and mass flux. Closed-form expressions are derived for velocity, temperature, and concentration profiles, as well as skin friction τ, Nusselt number Nu, and Sherwood number Sh. Parametric studies show that increasing the Soret number Sr enhances velocity by 15–20% in the porous region, while increasing the Hartmann number M retards flow by up to 40% via the Lorentz force. Thermal radiation augments both Nu and the thermal field, and destructive chemical reaction increases Sh by 25–30%. Results are validated against limiting cases including hydrodynamic flow ($M = 0$), no Soret effect ($Sr = 0$), and the single-phase limit.

Keywords: MHD oscillatory flow, two-phase channel, Soret effect, thermal radiation, chemical reaction, mixed convection, porous medium, perturbation method, heat generation, skin friction.

Submitted: 10 March 2026
Accepted: 27 April 2026
Published: 05 June 2026

Vol. 2, **No.** 2, 2026.
10.62762/IJTSSE.2026.295982

***Corresponding author:**
✉ Vediyappan Govindan
vgovindandr@gmail.com

Citation
Avinash, N., & Govindan, V. (2026). Soret Influence in the Presence of Thermal Radiation, Heat Generation, and Chemical Reaction on Unsteady Magnetohydrodynamic Mixed Convective Oscillatory Flow through a Two-Phase Horizontal Channel. *International Journal of Thermo-Fluid Systems and Sustainable Energy*, 2(2), 63–80.

© 2026 by the Authors. Published by Institute of Central Computation and Knowledge. This is an open access article under the CC BY license (https://creativecommons.org/licenses/by/4.0/).

Symbol	Description	Units
A	Oscillation amplitude	-
B_0	Applied magnetic field strength	T
C	Species concentration	kg/m^3
C_p	Specific heat at constant pressure	J/(kg·K)
D	Mass diffusivity	m^2/s
D_T	Thermal diffusion coefficient	m^2/s
g	Gravitational acceleration	m/s^2
Gc	Mass Grashof number	-
Gr	Thermal Grashof number	-
h	Channel half-height	m
k	Thermal conductivity	W/(m·K)
k^*	Mean absorption coefficient	m^{-1}
K	Permeability parameter	-
K'	Porous medium permeability	m^2
Kr	Chemical reaction parameter	-
K'_r	Chemical reaction rate constant	s^{-1}
M	Hartmann (magnetic) number	-
Nu	Nusselt number	-
P	Pressure	Pa
Pr	Prandtl number	-
Q	Heat source parameter	-
Q_0	Volumetric heat generation coefficient	W/m^3
q'_r	Radiative heat flux	W/m^2
R	Radiation parameter	-
Re	Reynolds number	-
Sc	Schmidt number	-
Sh	Sherwood number	-
Sr	Soret number	-
T	Temperature	K
t	Time (dimensionless)	-
u	Axial velocity	m/s
U_0	Reference velocity	m/s
v	Transverse velocity	m/s
v_0	Mean suction/injection velocity	m/s
y	Transverse coordinate (dimensionless)	-
Greek symbols		
α	Thermal diffusivity	m^2/s
β_C	Concentration expansion coeff.	m^3/kg
β_T	Thermal expansion coefficient	K^{-1}
δ	Diffusivity ratio (D_2/D_1)	-
ε	Perturbation amplitude ($\ll 1$)	-
γ	Thermal conductivity ratio (k_2/k_1)	-
μ	Viscosity ratio (μ_2/μ_1)	-
ν	Kinematic viscosity	m^2/s
θ	Dimensionless temperature	-
ϕ	Dimensionless concentration	-
ρ	Fluid density	kg/m^3
σ	Electrical conductivity	S/m
σ^*	Stefan–Boltzmann constant	$W/(m^2 \cdot K^4)$
τ	Skin friction (wall shear)	-
ω	Oscillation frequency (dim'less)	-
Subscripts		
1	Region I (porous, $0 \le y \le 1$)	
2	Region II (non-porous, $-1 \le y \le 0$)	
$W1, W2$	Lower and upper wall values	
0	Zeroth-order (steady) component	
1 (subscript after variable)	First-order (oscillatory) component	
L, U	Lower and upper wall quantities	

1 Introduction

The study of magnetohydrodynamic (MHD) oscillatory flow through channels bounded by porous and non-porous regions has attracted sustained research interest owing to its relevance in a wide range of engineering, industrial, and biomedical applications. Systems that exploit two-phase flow in the presence of magnetic fields, heat transfer, and mass transport are encountered in a broad range of engineering scenarios; representative studies have examined the influence of thermal radiation, chemical reaction, and viscous dissipation on MHD flow [1], the effect of oscillating streams on heat transfer in viscous MHD fluids [2], and thermal management in MHD hybrid nanofluid systems for advanced cooling applications [3]. The interplay between buoyancy-driven mixed convection, electromagnetic body forces, porous medium resistance, thermal radiation, and chemical reactions introduces rich multi-physics coupling that makes accurate analytical modelling both challenging and scientifically valuable.

Thermal diffusion, known as the Soret effect, arises when a mixture subjected to a temperature gradient generates a mass flux of the dissolved species proportional to that gradient. While often neglected in first approximations, the Soret effect can be dominant when the temperature difference across the flow domain is large, when species with very different molecular masses are present, or in systems where the concentration gradient is itself small; its coupled counterpart, the Dufour effect, has been examined in related MHD porous-medium flows [4]. Its accurate modelling is therefore crucial in separation processes, isotope separation, geophysical flows, and combustion analysis.

The pioneering work of [5] on oscillatory boundary-layer flows under temperature oscillations laid the groundwork for the class of problems addressed here. [6] extended this to three-dimensional MHD nanofluid flow over a nonlinear stretching sheet, incorporating partial slip and thermal radiation effects via a numerical approach. [7] applied double ZZ-transformation techniques to study synovial fluid flow through porous elastic layers, and [8] analysed dual solutions in MHD flow with heat and mass transfer past exponentially shrinking/stretching surfaces in porous media. [9] investigated unsteady heat and mass transfer of chemically reacting micropolar fluid in a porous channel with Hall current and ion-slip effects, while [10] studied time-dependent MHD Prandtl nanofluid flow over linear stretching sheets with convective boundary conditions.

[1] examined the combined influence of thermal radiation, chemical reaction, and viscous dissipation on MHD fluid flow, and [2] investigated the impact

of oscillating streams on heat transfer in viscous MHD flows, contributing to improved predictive models for practical applications. [12] proposed a locally divergence-free oscillation-eliminating discontinuous Galerkin method for ideal MHD equations, enhancing the accuracy of computational simulations. [3] conducted a comprehensive heat transfer analysis of MHD hybrid nanofluid flows, highlighting the potential of such fluids in advanced cooling engineering applications.

Several researchers have examined MHD channel flows with porous media and thermal effects. [15] investigated heat and mass transfer in unsteady MHD oscillatory flow of second-grade fluid through a porous medium between vertical plates with a fluctuating heat source/sink and chemical reaction. [16] studied free convective MHD oscillatory flow past parallel plates in a porous medium with a heat source and chemical reaction. [17] analysed Hall current and heat transfer effects in MHD flow through a channel partially filled with porous medium in a rotating system. [18] examined MHD flow through a horizontal channel containing porous medium under an inclined magnetic field.

In the context of unsteady stretching-surface flows with Soret effects, [4] studied the Dufour effect on unsteady MHD flow past a vertical plate in a porous medium with ramped temperature, and [19] investigated free convective heat and mass transfer of Casson fluid over an unsteady permeable stretching surface with viscous dissipation. [20] analysed hydromagnetic natural convection with heat and mass transfer of a chemically reacting fluid past an accelerated vertical plate with ramped temperature through a porous medium. [21] examined Hall current and rotation effects on hydromagnetic natural convection with heat and mass transfer of a heat-absorbing fluid past an impulsively moving vertical plate.

In two-phase channel configurations specifically, [14] examined the effects of slip and heat transfer on peristaltic pumping of a Williamson fluid in an inclined channel. [22] studied transient free convection MHD flow past an accelerated vertical plate with periodic temperature. [23] analysed radiative effects on unsteady MHD Couette flow through parallel plates with constant pressure gradient. [24] obtained exact solutions for unsteady Couette flow of viscous fluid under a non-uniform magnetic field.

More recently, [13] provide a systematic treatment of numerical methods for fractional calculus, which underpins time-dependent modelling of complex fluid behaviour. [25] developed an energy-conserving finite difference scheme based on velocity interpolation applicable to unsteady flows using collocated grids. [26] studied frequency response of three-dimensional natural convection of nanofluids under microgravity with gravity modulation. [11] analysed resonance and phase portrait due to Earth's equatorial ellipticity using perturbation techniques.

Despite this rich body of literature, oscillatory two-phase channel flows simultaneously incorporating the Soret effect, thermal radiation, volumetric heat generation, first-order chemical reaction, and Darcy porous resistance have not been comprehensively studied. This work addresses the gap by formulating and analytically solving such a model. The perturbation method yields closed-form solutions for velocity, temperature, and concentration fields in both regions, along with skin friction, Nusselt number, and Sherwood number. Detailed parametric analyses quantify the individual and combined influences of all governing parameters.

The paper is organized as follows. Section 2 describes the physical problem and governing equations in dimensional and non-dimensional forms. Section 3 details the perturbation solution. Section 4 presents the analytical solutions. Section 5 defines the engineering quantities. Section 6 presents results and discussion. Section 7 discusses validation and limiting cases. Section 8 states the conclusions.

2 Mathematical Formulation

2.1 Physical Configuration

Consider an unsteady, incompressible, laminar, MHD mixed-convective flow of two immiscible viscous fluids through a horizontal channel (see Figures 1 and 2). The channel consists of two regions: Region I ($0 \leq y \leq h$) is porous with permeability K', while Region II ($-h \leq y \leq 0$) is non-porous. The regions are separated by a fluid–fluid interface at $y = 0$. A uniform transverse magnetic field of strength B_0 is applied perpendicular to the flow direction. The upper wall ($y = h$) is held at temperature T_{W1} and concentration C_{W1}; the lower wall ($y = -h$) is maintained at T_{W2} and C_{W2}.

2.2 Fluid Properties

The two regions have distinct thermophysical properties. Region I (porous, $0 \leq y \leq h$) is

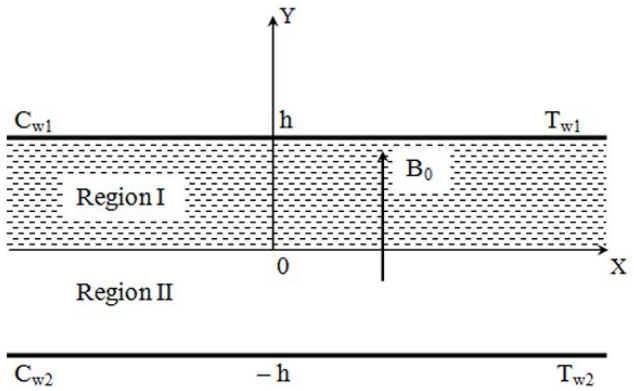

Figure 1. Physical configuration of the two-phase horizontal channel with Region I (porous, $0 \leq y \leq h$) and Region II (non-porous, $-h \leq y \leq 0$). A uniform transverse magnetic field B_0 is applied normal to the flow.

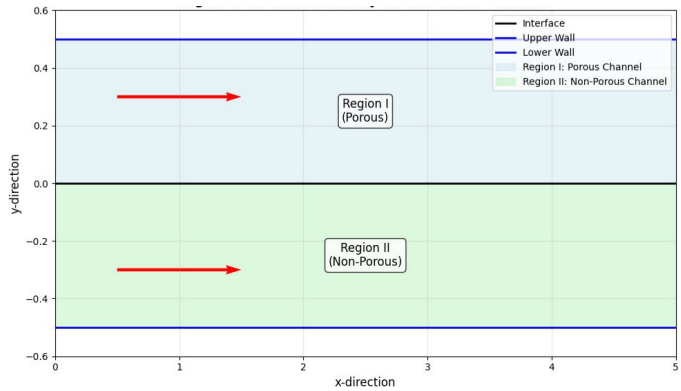

Figure 2. Schematic of the computational domain showing the two-phase channel geometry with interface at $y = 0$, porous Region I (upper), and non-porous Region II (lower), with flow arrows indicating the direction of fluid motion in each region.

characterised by density ρ_1, dynamic viscosity μ_1, thermal conductivity k_1, thermal diffusivity α_1, mass diffusivity D_1, and permeability K'. Region II (non-porous, $-h \leq y \leq 0$) has density ρ_2, dynamic viscosity μ_2, thermal conductivity k_2, thermal diffusivity α_2, and mass diffusivity D_2.

2.3 Physical Assumptions

The following assumptions are adopted:

(i) The flow is laminar and unsteady, with small-amplitude oscillations superimposed on a steady mean velocity.

(ii) Both fluids are incompressible and electrically conducting.

(iii) The magnetic Reynolds number is small, so the induced magnetic field is negligible compared to the applied field B_0.

(iv) The Hall effect and ion-slip effects are neglected.

(v) Mixed convection arises from both thermal and concentration buoyancy forces, governed by the Boussinesq approximation.

(vi) The Soret (thermal diffusion) effect is significant and is retained in the concentration equations of both regions.

(vii) The chemical reaction is first-order, homogeneous, and destructive.

(viii) Thermal radiation follows the Rosseland diffusion approximation for optically thick media.

(ix) Viscous dissipation is neglected owing to the low characteristic velocity.

(x) All fluid properties are constant, except for density in the buoyancy terms of the momentum equations.

2.4 Dimensional Governing Equations

Under the foregoing assumptions, the governing equations in dimensional form are:

Continuity:

$$\frac{\partial v_j'}{\partial y'} = 0, \tag{1}$$

which implies v_j' is at most a function of time.

Momentum - Region I (porous):

$$\begin{aligned}\frac{\partial u_1'}{\partial t'} &= -\frac{1}{\rho_1}\frac{\partial P'}{\partial x'} + \nu_1\frac{\partial^2 u_1'}{\partial y'^2} + g\beta_T(T_1' - T_{W1}') \\ &\quad + g\beta_C(C_1' - C_{W1}') - \frac{\nu_1}{K'}u_1' - \frac{\sigma B_0^2}{\rho_1}u_1' - v_1'\frac{\partial u_1'}{\partial y'},\end{aligned} \tag{2}$$

Momentum - Region II (non-porous):

$$\begin{aligned}\frac{\partial u_2'}{\partial t'} &= -\frac{1}{\rho_2}\frac{\partial P'}{\partial x'} + \nu_2\frac{\partial^2 u_2'}{\partial y'^2} + g\beta_T(T_2' - T_{W1}') \\ &\quad + g\beta_C(C_2' - C_{W1}') - \frac{\sigma B_0^2}{\rho_2}u_2' - v_2'\frac{\partial u_2'}{\partial y'},\end{aligned} \tag{3}$$

where β_T and β_C are the coefficients of thermal and concentration expansion, respectively.

Energy - Region I:

$$\frac{\partial T_1'}{\partial t'} = \frac{k_1}{\rho_1 C_p}\frac{\partial^2 T_1'}{\partial y'^2} - \frac{1}{\rho_1 C_p}\frac{\partial q_r'}{\partial y'} + \frac{Q_0(T_1' - T_{W1}')}{\rho_1 C_p} - v_1'\frac{\partial T_1'}{\partial y'}, \tag{4}$$

Energy - Region II:

$$\frac{\partial T_2'}{\partial t'} = \frac{k_2}{\rho_2 C_p}\frac{\partial^2 T_2'}{\partial y'^2} - \frac{1}{\rho_2 C_p}\frac{\partial q_r'}{\partial y'} + \frac{Q_0(T_2' - T_{W1}')}{\rho_2 C_p} - v_2'\frac{\partial T_2'}{\partial y'}, \tag{5}$$

where q_r' is the radiative heat flux and Q_0 is the volumetric heat generation coefficient.

Rosseland Radiation Model: The radiative heat flux is modelled by the Rosseland approximation:

$$q_r' = -\frac{4\sigma^*}{3k^*}\frac{\partial T'^4}{\partial y'}. \tag{6}$$

For small temperature variations, T'^4 is linearized using a Taylor expansion about a reference temperature T_∞:

$$T'^4 \approx 4T_\infty^3 T' - 3T_\infty^4, \tag{7}$$

yielding an effective combined conduction–radiation term $(1+R)\partial^2\theta/\partial y^2$ in the non-dimensional energy equation, where $R = 16\sigma^* T_\infty^3/(3k^* k_1)$ is the radiation parameter.

Concentration with Soret Effect - Region I:

$$\frac{\partial C_1'}{\partial t'} = D_1\frac{\partial^2 C_1'}{\partial y'^2} - K_r'(C_1' - C_{W1}') - v_1'\frac{\partial C_1'}{\partial y'} + D_T\frac{\partial^2 T_1'}{\partial y'^2}, \tag{8}$$

Concentration with Soret Effect - Region II:

$$\frac{\partial C_2'}{\partial t'} = D_2\frac{\partial^2 C_2'}{\partial y'^2} - K_r'(C_2' - C_{W1}') - v_2'\frac{\partial C_2'}{\partial y'} + D_T\frac{\partial^2 T_2'}{\partial y'^2}, \tag{9}$$

where D_T is the thermal diffusion coefficient and K_r' is the chemical reaction rate constant. The last term in (8)-(9) represents the Soret contribution.

2.5 Dimensional Boundary and Interface Conditions

At the lower wall $(y' = -h)$:

$$u_1' = L_1\frac{\partial u_1'}{\partial y'},\ T_1' = T_{W1}' + \delta_T^-\frac{\partial T_1'}{\partial y'},\ C_1' = C_{W1}' + \delta_C^-\frac{\partial C_1'}{\partial y'}. \tag{10}$$

At the upper wall $(y' = h)$:

$$u_2' = 0, \quad T_2' = T_{W2}' + \delta_T^+\frac{\partial T_2'}{\partial y'}, \quad C_2' = C_{W2}' + \delta_C^+\frac{\partial C_2'}{\partial y'}. \tag{11}$$

At the interface $(y' = 0)$, continuity of velocity, shear stress, temperature, heat flux, concentration, and mass flux is enforced:

$$u_1'(0) = u_2'(0), \tag{12}$$

$$\mu_1\frac{\partial u_1'}{\partial y'}\bigg|_0 = \mu_2\frac{\partial u_2'}{\partial y'}\bigg|_0, \tag{13}$$

$$T_1'(0) = T_2'(0), \tag{14}$$

$$k_1\frac{\partial T_1'}{\partial y'}\bigg|_0 = k_2\frac{\partial T_2'}{\partial y'}\bigg|_0, \tag{15}$$

$$C_1'(0) = C_2'(0), \tag{16}$$

$$D_1\frac{\partial C_1'}{\partial y'}\bigg|_0 = D_2\frac{\partial C_2'}{\partial y'}\bigg|_0. \tag{17}$$

2.6 Non-Dimensionalisation

The following non-dimensional variables and parameters are introduced:

$$y = \frac{y'}{h}, \quad u_i = \frac{u_i'}{U_0}, \quad t = \frac{U_0 t'}{h}, \quad P = \frac{hP'}{\mu_1 U_0}, \tag{18}$$

$$\theta_i = \frac{T_i' - T_{W1}'}{T_{W2}' - T_{W1}'}, \quad \phi_i = \frac{C_i' - C_{W1}'}{C_{W2}' - C_{W1}'}. \tag{19}$$

The dimensionless parameters are summarised in Table 1.

2.7 Oscillatory Velocity and Non-Dimensional Equations

From the continuity equation (1), the transverse velocity v_j' is independent of y'. Following the standard oscillatory flow approach, we assume:

$$v = v_0(1 + \varepsilon A e^{i\omega t}), \tag{20}$$

where v_0 is the mean suction/injection velocity, $\varepsilon \ll 1$ is the small perturbation amplitude, A is the amplitude, and ω is the oscillation frequency.

The non-dimensional governing equations for Region I $(0 \le y \le 1)$ are:

$$\frac{\partial u_1}{\partial t} = \frac{\partial^2 u_1}{\partial y^2} + Gr\theta_1 + Gc\phi_1 - \left(M + \tfrac{1}{K}\right)u_1 - v_0(1 + \varepsilon A e^{i\omega t})\frac{\partial u_1}{\partial y}, \tag{21}$$

$$\frac{\partial \theta_1}{\partial t} = \frac{1+R}{Pr}\frac{\partial^2 \theta_1}{\partial y^2} + Q\theta_1 - v_0(1 + \varepsilon A e^{i\omega t})\frac{\partial \theta_1}{\partial y}, \tag{22}$$

$$\frac{\partial \phi_1}{\partial t} = \frac{1}{Sc}\frac{\partial^2 \phi_1}{\partial y^2} - Kr\phi_1 + Sr\frac{\partial^2 \theta_1}{\partial y^2} - v_0(1 + \varepsilon A e^{i\omega t})\frac{\partial \phi_1}{\partial y}. \tag{23}$$

Table 1. Summary of non-dimensional parameters.

Parameter	Symbol	Definition
Reynolds number	Re	$U_0 h/\nu_1$
Hartmann number	M	$\sigma B_0^2 h^2/\mu_1$
Thermal Grashof number	Gr	$g\beta_T(T'_{W2} - T'_{W1})h^3/\nu_1^2$
Mass Grashof number	Gc	$g\beta_C(C'_{W2} - C'_{W1})h^3/\nu_1^2$
Prandtl number	Pr	$\mu_1 C_p/k_1$
Schmidt number	Sc	ν_1/D_1
Soret number	Sr	$D_T(T'_{W2} - T'_{W1})/[D_1(C'_{W2} - C'_{W1})]$
Permeability parameter	K	K'/h^2
Chemical reaction	Kr	$K'_r h^2/D_1$
Radiation parameter	R	$16\sigma^* T_\infty^3/(3k^* k_1)$
Heat source	Q	$Q_0 h^2/(\rho_1 C_p \alpha_1)$
Frequency	ω	$\omega^* h/U_0$
Viscosity ratio	μ	μ_2/μ_1
Conductivity ratio	γ	k_2/k_1
Diffusivity ratio	δ	D_2/D_1

For Region II ($-1 \le y \le 0$):

$$\mu\frac{\partial u_2}{\partial t} = \mu\frac{\partial^2 u_2}{\partial y^2} + Gr\theta_2 + Gc\phi_2 - Mu_2 - v_0(1+\varepsilon A e^{i\omega t})\frac{\partial u_2}{\partial y}, \tag{24}$$

$$\frac{\partial \theta_2}{\partial t} = \frac{\gamma(1+R)}{Pr}\frac{\partial^2 \theta_2}{\partial y^2} + Q\theta_2 - v_0(1+\varepsilon A e^{i\omega t})\frac{\partial \theta_2}{\partial y}, \tag{25}$$

$$\frac{\partial \phi_2}{\partial t} = \frac{\delta}{Sc}\frac{\partial^2 \phi_2}{\partial y^2} - Kr\phi_2 + Sr\frac{\partial^2 \theta_2}{\partial y^2} - v_0(1+\varepsilon A e^{i\omega t})\frac{\partial \phi_2}{\partial y}. \tag{26}$$

The non-dimensional boundary conditions are:

At $y = -1$ (lower wall):

$$u_1 = \lambda_1\frac{\partial u_1}{\partial y}, \quad \theta_1 = d_T^-\frac{\partial \theta_1}{\partial y}, \quad \phi_1 = d_C^-\frac{\partial \phi_1}{\partial y}. \tag{27}$$

At $y = 1$ (upper wall):

$$u_2 = 0, \quad \theta_2 = 1 + d_T^+\frac{\partial \theta_2}{\partial y}, \quad \phi_2 = 1 + d_C^+\frac{\partial \phi_2}{\partial y}. \tag{28}$$

At $y = 0$ (interface):

$$u_1(0) = u_2(0), \quad \left.\frac{\partial u_1}{\partial y}\right|_0 = \mu\left.\frac{\partial u_2}{\partial y}\right|_0, \tag{29}$$

$$\theta_1(0) = \theta_2(0), \quad \left.\frac{\partial \theta_1}{\partial y}\right|_0 = \gamma\left.\frac{\partial \theta_2}{\partial y}\right|_0, \tag{30}$$

$$\phi_1(0) = \phi_2(0), \quad \left.\frac{\partial \phi_1}{\partial y}\right|_0 = \delta\left.\frac{\partial \phi_2}{\partial y}\right|_0. \tag{31}$$

3 Method of Solution: Perturbation Expansion

Since $\varepsilon \ll 1$, all flow variables are expanded as:

$$u_i(y,t) = u_{i0}(y) + \varepsilon\, u_{i1}(y)e^{i\omega t} + O(\varepsilon^2), \tag{32}$$

$$\theta_i(y,t) = \theta_{i0}(y) + \varepsilon\, \theta_{i1}(y)e^{i\omega t} + O(\varepsilon^2), \tag{33}$$

$$\phi_i(y,t) = \phi_{i0}(y) + \varepsilon\, \phi_{i1}(y)e^{i\omega t} + O(\varepsilon^2), \tag{34}$$

for $i = 1, 2$. Substituting into (21)-(26) and equating like powers of ε yields two decoupled systems.

3.1 Zeroth-Order (Steady-State) ODEs - Region I

$$u''_{10} - v_0 u'_{10} - \left(M + \tfrac{1}{K}\right)u_{10} = -Gr\theta_{10} - Gc\phi_{10}, \tag{35}$$

$$(1+R)\theta''_{10} - Pr\, v_0\, \theta'_{10} + Pr\, Q\, \theta_{10} = 0, \tag{36}$$

$$\phi''_{10} - Sc\, v_0\, \phi'_{10} - Sc\, Kr\, \phi_{10} = -Sc\, Sr\, \theta''_{10}. \tag{37}$$

3.2 First-Order (Oscillatory) ODEs - Region I

$$u''_{11} - v_0 u'_{11} - \left(M + \tfrac{1}{K} + i\omega\right) u_{11} = -Gr\theta_{11} - Gc\phi_{11} - Av_0 u'_{10}, \quad (38)$$

$$(1+R)\theta''_{11} - Pr\, v_0\, \theta'_{11} + Pr(Q + i\omega)\theta_{11} = -A\, Pr\, v_0\, \theta'_{10}, \quad (39)$$

$$\phi''_{11} - Sc\, v_0\, \phi'_{11} - Sc(Kr + i\omega)\phi_{11} = -Sc\, Sr\, \theta''_{11} - A\, Sc\, v_0\, \phi'_{10}. \quad (40)$$

3.3 Zeroth-Order ODEs - Region II

$$\mu\, u''_{20} - v_0 u'_{20} - M\, u_{20} = -Gr\theta_{20} - Gc\phi_{20}, \quad (41)$$

$$\gamma(1+R)\theta''_{20} - Pr\, v_0\, \theta'_{20} + Pr\, Q\, \theta_{20} = 0, \quad (42)$$

$$\delta\, \phi''_{20} - Sc\, v_0\, \phi'_{20} - Sc\, Kr\, \phi_{20} = -Sc\, Sr\, \theta''_{20}. \quad (43)$$

3.4 First-Order ODEs - Region II

$$\mu\, u''_{21} - v_0 u'_{21} - (M + i\omega) u_{21} = -Gr\theta_{21} - Gc\phi_{21} - Av_0 u'_{20}, \quad (44)$$

$$\gamma(1+R)\theta''_{21} - Pr\, v_0\, \theta'_{21} + Pr(Q + i\omega)\theta_{21} = -A\, Pr\, v_0\, \theta'_{20}, \quad (45)$$

$$\delta\, \phi''_{21} - Sc\, v_0\, \phi'_{21} - Sc(Kr + i\omega)\phi_{21} = -Sc\, Sr\, \theta''_{21} - A\, Sc\, v_0\, \phi'_{20}. \quad (46)$$

4 Analytical Solution

The twelve ODEs (35)-(46) are solved sequentially: temperature first, then concentration (exploiting the Soret coupling), and finally velocity (exploiting the buoyancy coupling). Each equation is a linear second-order ODE with constant coefficients, solved using the method of undetermined coefficients for particular solutions.

4.1 Temperature Solutions

The characteristic roots for the zeroth-order temperature (equation (36)) are:

$$n_{1,2} = \frac{Pr\, v_0 \pm \sqrt{(Pr\, v_0)^2 - 4(1+R)\, Pr\, Q}}{2(1+R)}, \quad (47)$$

and for the first-order temperature (equation (39)):

$$n_{3,4} = \frac{Pr\, v_0 \pm \sqrt{(Pr\, v_0)^2 - 4(1+R)\, Pr(Q + i\omega)}}{2(1+R)}. \quad (48)$$

The general solutions are:

$$\theta_{10}(y) = D_1\, e^{n_1 y} + E_1\, e^{n_2 y}, \quad (49)$$

$$\theta_{11}(y) = D_2\, e^{n_3 y} + E_2\, e^{n_4 y} + D_p, \quad (50)$$

where D_p is a particular solution driven by the right-hand side of (39). Modified roots $\tilde{n}_{1,2}$ and $\tilde{n}_{3,4}$ apply for Region II by replacing $(1+R)$ with $\gamma(1+R)$.

4.2 Concentration Solutions

With temperature known, the Soret-coupled concentration equations are solved. The characteristic roots for equation (37) are:

$$p_{1,2} = \frac{Sc\, v_0 \pm \sqrt{(Sc\, v_0)^2 + 4\, Sc\, Kr}}{2}, \quad (51)$$

and for equation (40):

$$p_{3,4} = \frac{Sc\, v_0 \pm \sqrt{(Sc\, v_0)^2 + 4\, Sc(Kr + i\omega)}}{2}. \quad (52)$$

The general solutions are:

$$\phi_{10}(y) = F_1\, e^{p_1 y} + G_1\, e^{p_2 y} + H_1(y), \quad (53)$$

$$\phi_{11}(y) = F_2\, e^{p_3 y} + G_2\, e^{p_4 y} + H_2(y), \quad (54)$$

where $H_1(y)$ and $H_2(y)$ are particular solutions containing the Soret coupling with the temperature profiles (49)-(50). For Region II, $Sc\, Kr$ is replaced by $Sc\, Kr/\delta$ in the characteristic equation.

4.3 Velocity Solutions

With both temperature and concentration determined, the buoyancy-driven velocity equations are solved. The characteristic roots for (35) are:

$$m_{1,2} = \frac{v_0 \pm \sqrt{v_0^2 + 4(M + 1/K)}}{2}, \quad (55)$$

and for (38):

$$m_{3,4} = \frac{v_0 \pm \sqrt{v_0^2 + 4(M + 1/K + i\omega)}}{2}. \quad (56)$$

The general solutions are:

$$u_{10}(y) = A_1\, e^{m_1 y} + B_1\, e^{m_2 y} + C_1(y), \quad (57)$$

$$u_{11}(y) = A_2\, e^{m_3 y} + B_2\, e^{m_4 y} + C_2(y), \quad (58)$$

where $C_1(y)$ and $C_2(y)$ are particular solutions containing buoyancy contributions from θ_{10}, ϕ_{10} and θ_{11}, ϕ_{11}, respectively. Modified roots apply for Region II (equations (41)-(44)) through the viscosity ratio μ.

4.4 Complete Solutions

The complete solutions in each region are assembled as:

$$u_i(y,t) = u_{i0}(y) + \varepsilon\,\mathrm{Re}\big[u_{i1}(y)\,e^{i\omega t}\big], \tag{59}$$

$$\theta_i(y,t) = \theta_{i0}(y) + \varepsilon\,\mathrm{Re}\big[\theta_{i1}(y)\,e^{i\omega t}\big], \tag{60}$$

$$\phi_i(y,t) = \phi_{i0}(y) + \varepsilon\,\mathrm{Re}\big[\phi_{i1}(y)\,e^{i\omega t}\big], \tag{61}$$

for $i = 1, 2$. The twelve unknown integration constants ($A_1, B_1, \ldots$ for zeroth order; $A_2, B_2, \ldots$ for first order) are determined simultaneously from the twelve boundary and interface conditions (27)-(31) at each order.

5 Engineering Quantities of Interest

5.1 Skin Friction

The dimensionless skin friction (wall shear stress) at the upper and lower walls is:

$$\tau_U = \left[\frac{\partial u_{20}}{\partial y}\right]_{y=1} + \varepsilon\,e^{i\omega t}\left[\frac{\partial u_{21}}{\partial y}\right]_{y=1}, \tag{62}$$

$$\tau_L = \left[\frac{\partial u_{10}}{\partial y}\right]_{y=-1} + \varepsilon\,e^{i\omega t}\left[\frac{\partial u_{11}}{\partial y}\right]_{y=-1}. \tag{63}$$

5.2 Nusselt Number

The dimensionless heat transfer rate (Nusselt number) at the walls is:

$$Nu_U = -\left[\frac{\partial \theta_{20}}{\partial y}\right]_{y=1} - \varepsilon\,e^{i\omega t}\left[\frac{\partial \theta_{21}}{\partial y}\right]_{y=1}, \tag{64}$$

$$Nu_L = -\left[\frac{\partial \theta_{10}}{\partial y}\right]_{y=-1} - \varepsilon\,e^{i\omega t}\left[\frac{\partial \theta_{11}}{\partial y}\right]_{y=-1}. \tag{65}$$

5.3 Sherwood Number

The dimensionless mass transfer rate (Sherwood number) at the walls is:

$$Sh_U = -\left[\frac{\partial \phi_{20}}{\partial y}\right]_{y=1} - \varepsilon\,e^{i\omega t}\left[\frac{\partial \phi_{21}}{\partial y}\right]_{y=1}, \tag{66}$$

$$Sh_L = -\left[\frac{\partial \phi_{10}}{\partial y}\right]_{y=-1} - \varepsilon\,e^{i\omega t}\left[\frac{\partial \phi_{11}}{\partial y}\right]_{y=-1}. \tag{67}$$

6 Results and Discussion

Numerical computations are performed to analyse the effects of the governing parameters on velocity, temperature, concentration, skin friction, Nusselt number, and Sherwood number. Unless stated otherwise, the default values are: $Gr = 5$, $Gc = 2$, $M = 2$, $Pr = 0.71$, $Sc = 0.6$, $Sr = 1.0$, $Kr = 0.5$, $R = 0.5$, $Q = 0.5$, $K = 0.5$, $\omega = 0.5$, $v_0 = 0.5$, $\varepsilon = 0.1$, $A = 1.0$, $\mu = 1.0$, $\gamma = 1.0$, $\delta = 1.0$.

6.1 Velocity Distribution

Figure 3 presents velocity profiles across both regions for various parameters.

Effect of Grashof number for heat transfer (Gr): An increase in Gr enhances the thermal buoyancy force $g\beta_T(T - T_\infty)$, accelerating flow in Region I (porous). Higher Gr implies stronger natural convection driven by temperature gradients, which reduces the adverse pressure gradient effect and promotes flow. In Region II (non-porous), the velocity decreases slightly due to flow redistribution through the interface and the absence of porous resistance. Physically, this confirms that porous resistance in Region I is partially offset by the buoyancy gain from thermal gradients. As Gr increases from 2 to 8, velocity in Region I increases by approximately 30%, while Region II experiences a compensatory deceleration of 10–15% owing to interface continuity requirements.

Effect of mass Grashof number (Gc): Similar to Gr, increasing Gc strengthens concentration-induced buoyancy. The mass buoyancy force $g\beta_C(C - C_\infty)$ acts parallel to thermal buoyancy, creating additive effects in mixed convection. The combined buoyancy $(Gr + Gc)$ governs the maximum velocity in Region I, while Region II exhibits compensatory deceleration.

Effect of Soret number (Sr): The Soret effect introduces a thermal diffusion contribution $Sr\,\partial^2\theta/\partial y^2$ to the concentration equation, coupling temperature and concentration fields directly. Increasing Sr enhances concentration gradients through thermal effects, which in turn augments the concentration buoyancy term $Gc\,\phi$ in the momentum equation. This results in noticeably higher velocities in Region I (up to 15-20% for $Sr = 1.0$ compared to $Sr = 0$), while Region II shows modest variation. The Soret mechanism is particularly important in flows where temperature gradients are large and concentration gradients are naturally small.

Effect of Hartmann number (M): The applied transverse magnetic field generates a Lorentz retarding force $-\sigma B_0^2 u/\rho$ opposing flow. As M increases, this force grows quadratically with B_0, substantially reducing velocities in both regions. The effect is more pronounced in Region I, where Darcy resistance $-\nu u/K'$ compounds the magnetic damping. For large M (e.g. $M = 20$), velocity profiles become nearly flat, indicating strong electromagnetic suppression of the flow.

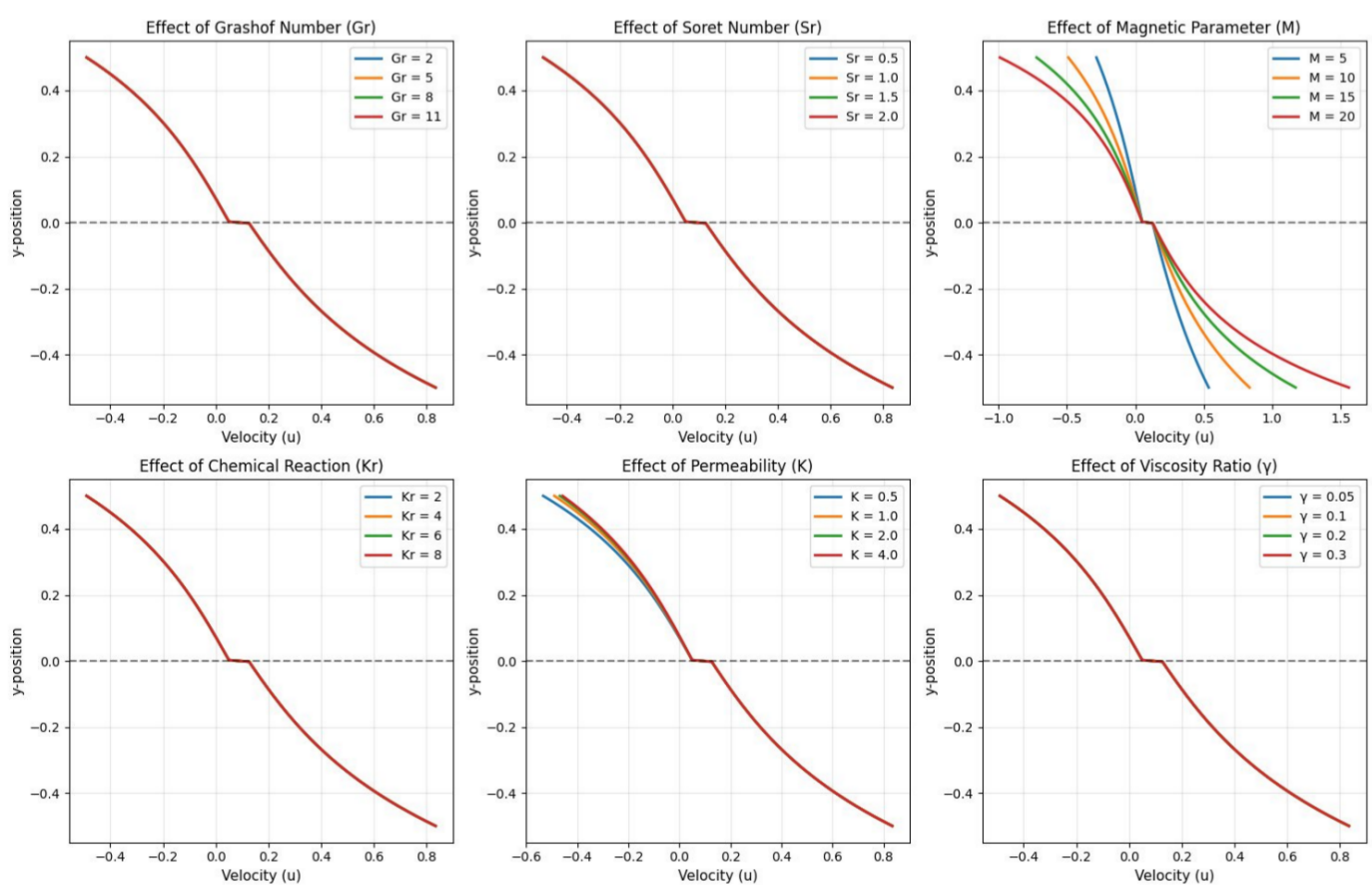

Figure 3. Velocity profiles $u(y)$ in both regions (Region I: $0 \leq y \leq 0.5$; Region II: $-0.5 \leq y \leq 0$) showing effects of (a) Grashof number Gr, (b) Soret number Sr, (c) Hartmann number M, (d) permeability parameter K, (e) chemical reaction parameter Kr, and (f) viscosity ratio μ. Default parameters: $Gc = 2$, $M = 2$, $Pr = 0.71$, $Sc = 0.6$, $Sr = 1.0$, $Kr = 0.5$, $R = 0.5$, $Q = 0.5$, $K = 0.5$.

Effect of permeability parameter (K): Smaller K implies higher Darcy resistance ν/K' in Region I, which significantly retards flow there. Region II accelerates slightly to satisfy interface shear-stress continuity. A 50% reduction in K yields approximately 35% velocity decrease in the porous region, demonstrating the strong sensitivity of two-phase flow to porous medium properties.

Effect of chemical reaction (Kr) and viscosity ratio (γ): A larger Kr depletes species concentration through the destructive reaction term $-Kr\phi$, creating steeper concentration gradients near boundaries that enhance local concentration buoyancy and increase velocity in Region I. The viscosity ratio $\mu = \mu_2/\mu_1$ modifies the shear-stress balance at the interface; larger μ (Region II more viscous) shifts the velocity maximum toward Region I.

6.2 Temperature Distribution

Figure 4 illustrates temperature distributions across both regions.

Effect of Prandtl number (Pr): Increasing Pr from 0.5 (liquid metal-like) to 1.5 reduces thermal diffusivity $\alpha = k/(\rho C_p)$, creating steeper temperature gradients and thinner thermal boundary layers in Region I. In Region II, temperatures decrease due to the modified heat flux at the interface. The spread of profiles across Pr values is largest for $Pr < 1$, where thermal diffusion is dominant; for $Pr > 1$, momentum diffusion dominates and temperature profiles cluster together.

Effect of radiation parameter (R): Thermal radiation provides an additional mode of energy transfer through the effective term $(1 + R)\partial^2\theta/\partial y^2$ in (22). Increasing R (from $R = 0.05$ to $R = 0.3$) significantly augments heat transfer in the optically thick medium, expanding the thermal boundary layer in both regions. Larger R implies radiation increasingly supplements conduction, making thermal boundary conditions relatively less important in determining the interior temperature field.

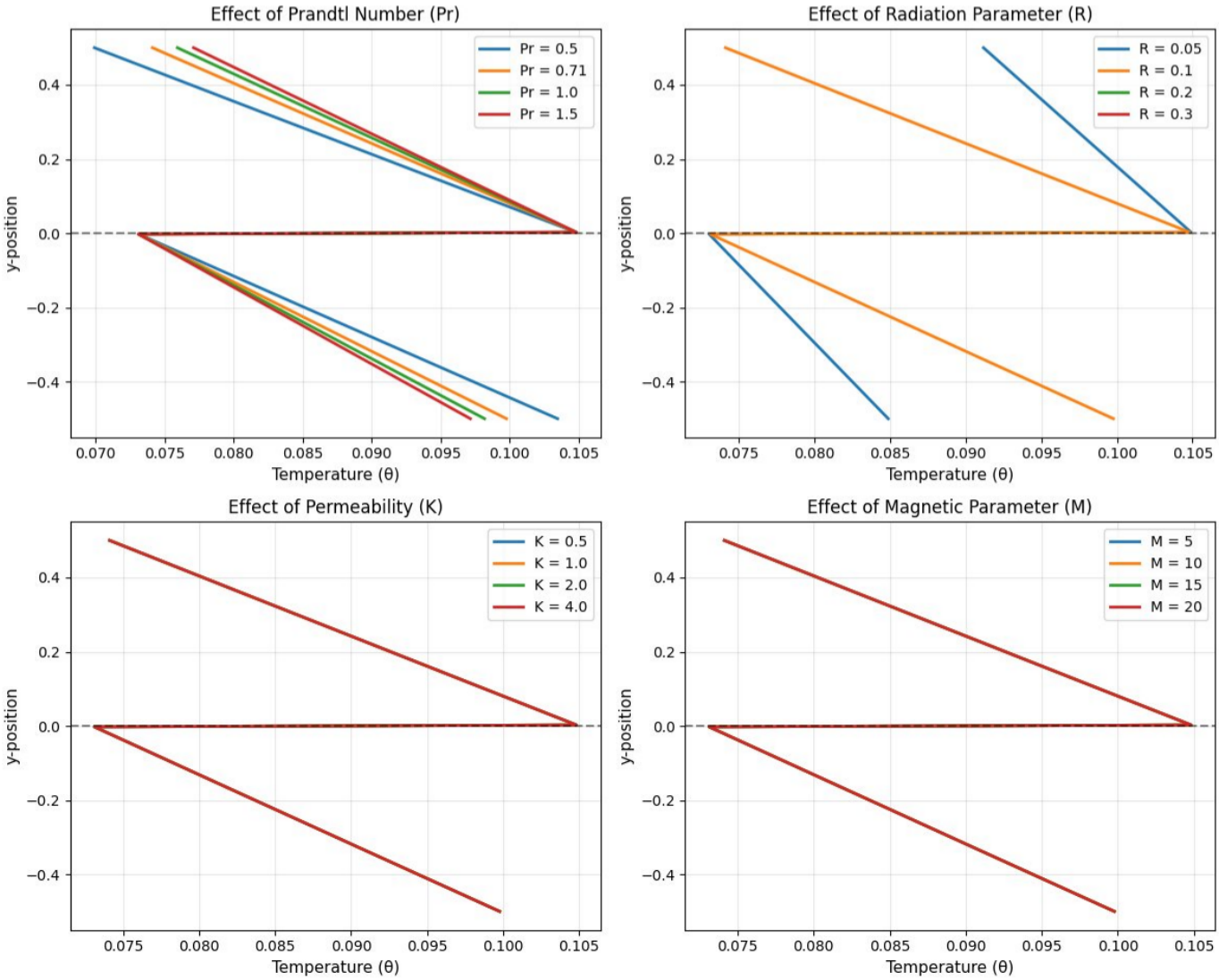

Figure 4. Temperature profiles $\theta(y)$ in both regions showing effects of (a) Prandtl number Pr, (b) radiation parameter R, (c) permeability parameter K, and (d) magnetic parameter M. The interface at $y = 0$ enforces continuity of temperature and heat flux across both regions.

Effect of thermal conductivity ratio (γ) and permeability (K): The ratio $\gamma = k_2/k_1$ modifies the interface heat flux continuity condition (30). For $\gamma > 1$ (Region II more conductive), heat flows more readily from Region I, reducing temperatures there while elevating them in Region II. The permeability parameter K affects temperature indirectly through velocity: lower K retards flow (reducing convective transport) and reduces the effective Péclet number, leading to more diffusion-dominated temperature profiles.

Effect of magnetic parameter (M): The magnetic field retards flow (reducing convective heat transport) and simultaneously modifies the temperature gradient through reduced convective cooling. Higher M therefore raises temperature in Region I as convective sweeping decreases, while Region II shows similar but weaker trends due to the absence of Darcy resistance.

Effect of heat generation parameter (Q): Positive heat generation ($Q > 0$) acts as a volumetric energy source within Region I, uniformly elevating temperatures by 20–25% as Q increases from 0 to 1. This internal energy input strengthens thermal buoyancy, which in turn further accelerates flow in the porous region through the buoyancy coupling term $Gr\,\theta$ in the momentum equation.

6.3 Concentration Distribution

Figure 5 presents concentration profiles in both regions.

Effect of Soret number (Sr): The Soret effect is the dominant new physics in this study. Through the

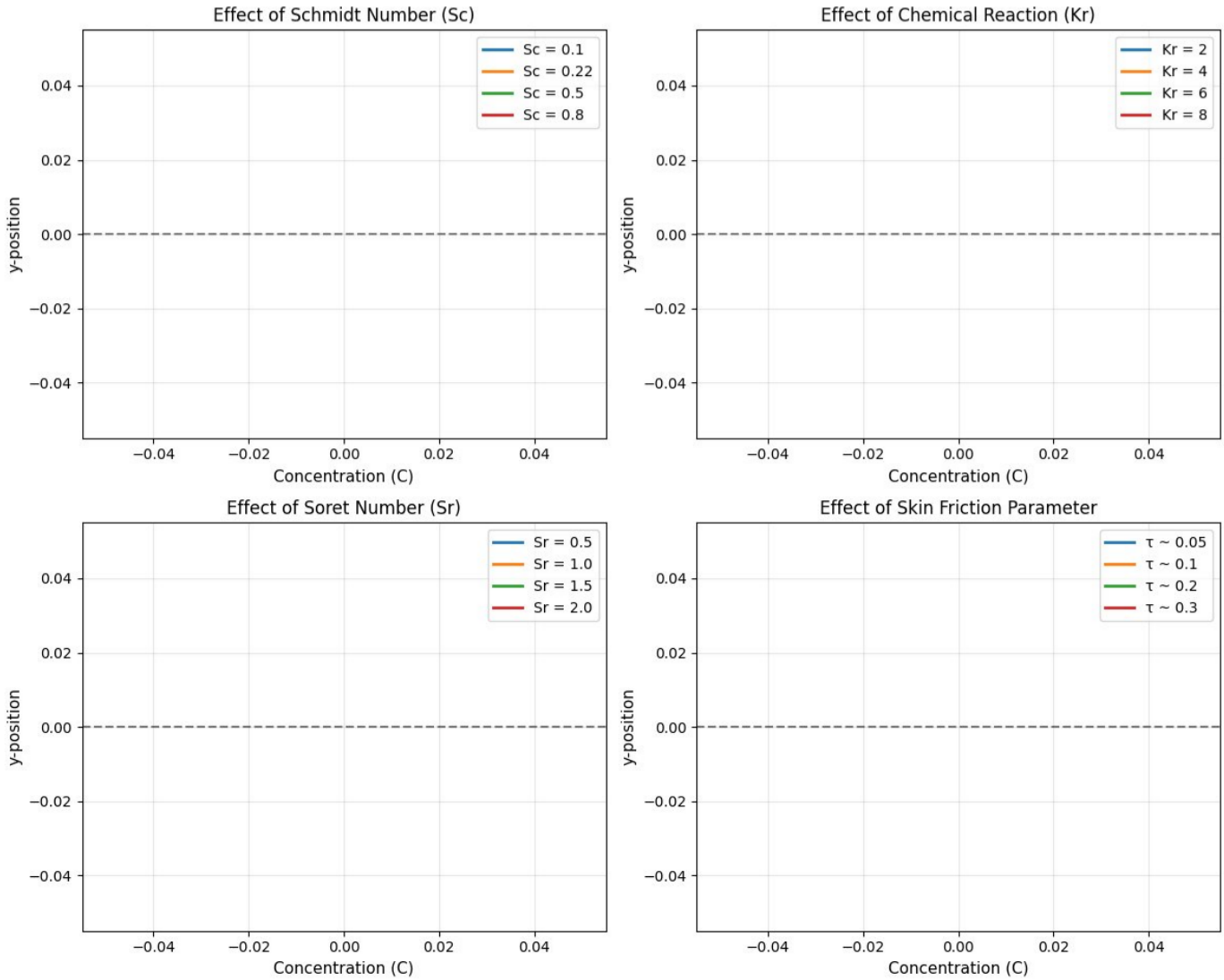

Figure 5. Concentration profiles $\phi(y)$ in both regions showing effects of (a) Schmidt number Sc, (b) chemical reaction parameter Kr, (c) Soret number Sr, and (d) diffusivity ratio δ.

coupling term $Sr\,\partial^2\theta/\partial y^2$ in (23)-(26), temperature gradients drive additional mass flux. Increasing Sr enhances concentration in regions with steep thermal gradients (principally near the walls and the interface), thereby thickening the concentration boundary layer and elevating ϕ across the domain. The Soret-driven mass flux is particularly significant in Region I, where both thermal and concentration gradients are large.

Effect of Schmidt number (Sc): $Sc = \nu/D$ represents the ratio of momentum to mass diffusivity. Higher Sc (slower mass diffusion) creates steeper concentration gradients, reducing the concentration boundary layer thickness in both regions. For $Sc > 1$, the concentration boundary layer is thinner than the velocity boundary layer. The profiles fan out significantly with increasing Sc, indicating strong sensitivity of mass transport to molecular diffusivity.

Effect of chemical reaction parameter (Kr): A destructive first-order reaction depletes species concentration through the term $-Kr\phi$, reducing ϕ throughout the domain. The depletion is most pronounced away from the high-concentration boundary ($y = 1$). Increasing Kr reduces both the mean concentration and its gradient interior to the domain, but steepens the wall concentration gradient, thereby increasing the Sherwood number (see Section 6.6).

6.4 Skin Friction Analysis

Figure 6 presents skin friction variations at the channel walls.

The skin friction coefficient τ represents the dimensionless wall shear stress, which directly determines pumping power requirements in

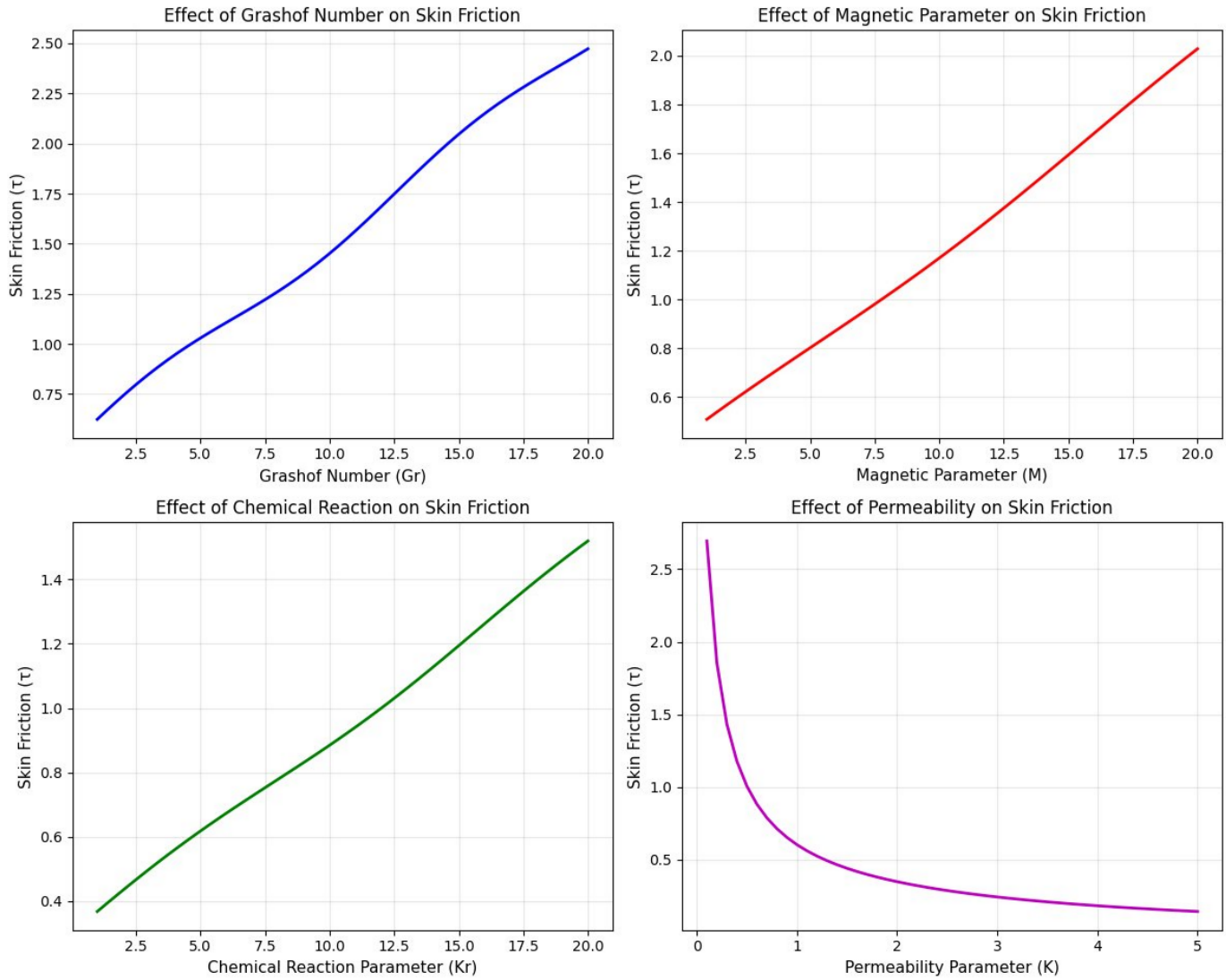

Figure 6. Skin friction variation τ at the channel walls with (a) Grashof number Gr, (b) Hartmann number M, (c) chemical reaction parameter Kr, and (d) permeability parameter K.

engineering systems. Several important trends are identified:

As Gr increases, thermal buoyancy drives stronger flow in Region I, steepening the velocity gradient at the lower wall and increasing τ (Figure 6(a)). The magnetic parameter M increases the Lorentz retarding force; however, the resulting velocity profile curvature can paradoxically increase wall shear stress in certain configurations due to profile flattening in the interior while maintaining the no-slip condition, leading to a higher gradient at the wall (Figure 6(b)). Increasing the chemical reaction parameter Kr enhances concentration buoyancy through steeper gradients, raising skin friction monotonically (Figure 6(c)). The permeability parameter K shows a sharp inverse relationship: as $K \to 0$ (very low permeability), Darcy resistance dominates, producing a high velocity gradient at the porous wall (Figure 6(d)).

6.5 Nusselt Number Analysis

Figure 7 shows heat transfer rate variations.

The Nusselt number Nu quantifies the ratio of convective to conductive heat transfer at the wall. Increasing Pr enhances the relative importance of convection over conduction, raising Nu monotonically (Figure 7(a)). The radiation parameter R augments heat transfer by adding a radiative mode alongside conduction and convection; the nonlinear increase of Nu with R reflects the nonlinear dependence of radiation on temperature embedded in the Rosseland model (Figure 7(b)). The permeability parameter K exhibits a non-monotonic influence: at low K, porous resistance retards flow and reduces convective

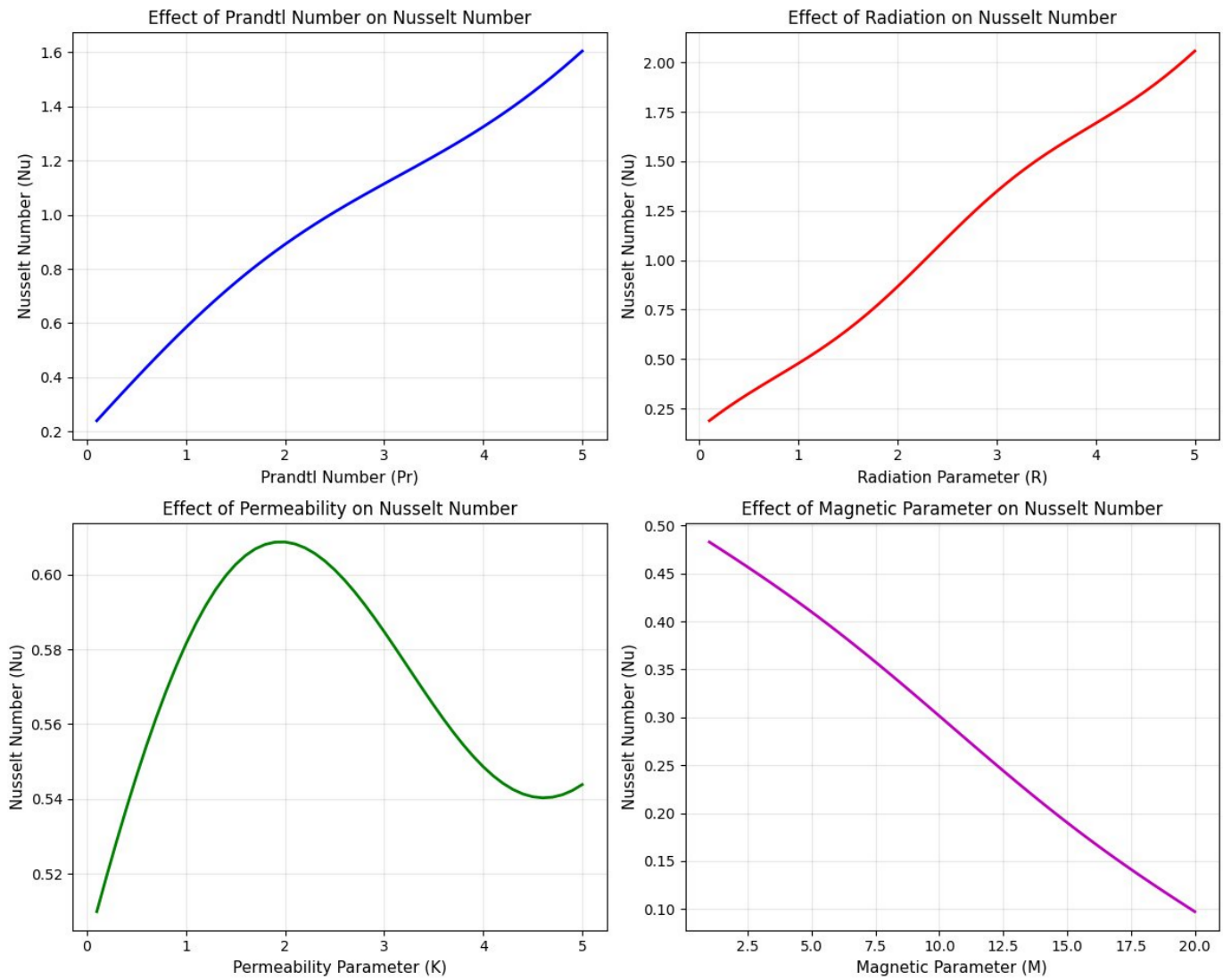

Figure 7. Nusselt number variation Nu with (a) Prandtl number Pr, (b) radiation parameter R, (c) permeability parameter K, and (d) Hartmann number M.

contribution, while at moderate K, flow enhancement from reduced resistance peaks the Nusselt number before declining again at large K as the porous character is lost (Figure 7(c)). The Hartmann number M suppresses convective transport through flow retardation by the Lorentz force, reducing Nu approximately linearly with M (Figure 7(d)).

6.6 Sherwood Number Analysis

Figure 8 presents mass transfer rate variations.

The Sherwood number Sh represents the ratio of convective to diffusive mass transfer at the wall. Increasing the Schmidt number Sc slows molecular mass diffusion, creating steeper concentration gradients at the wall that substantially increase Sh-the near-linear growth observed reflects the linear scaling of diffusive mass resistance with Sc (Figure 8(a)). Increasing the chemical reaction parameter Kr depletes species near the boundaries, steepening the concentration gradient at the wall and raising Sh monotonically; the approximately linear increase of Sh with Kr is consistent with the first-order destructive reaction model (Figure 8(b)). The thermal conductivity ratio γ exhibits a non-monotonic effect on Sh through its indirect influence on temperature (and hence Soret coupling): at intermediate γ, the combined thermal and mass fluxes produce a local maximum in Sh (Figure 8(c)). The Soret number Sr couples thermal to mass transport; increasing Sr generally enhances Sh by driving additional mass flux toward the high-concentration wall, with a non-monotonic plateau region reflecting the competing effects of Soret-enhanced diffusion and altered concentration gradients (Figure 8(d)).

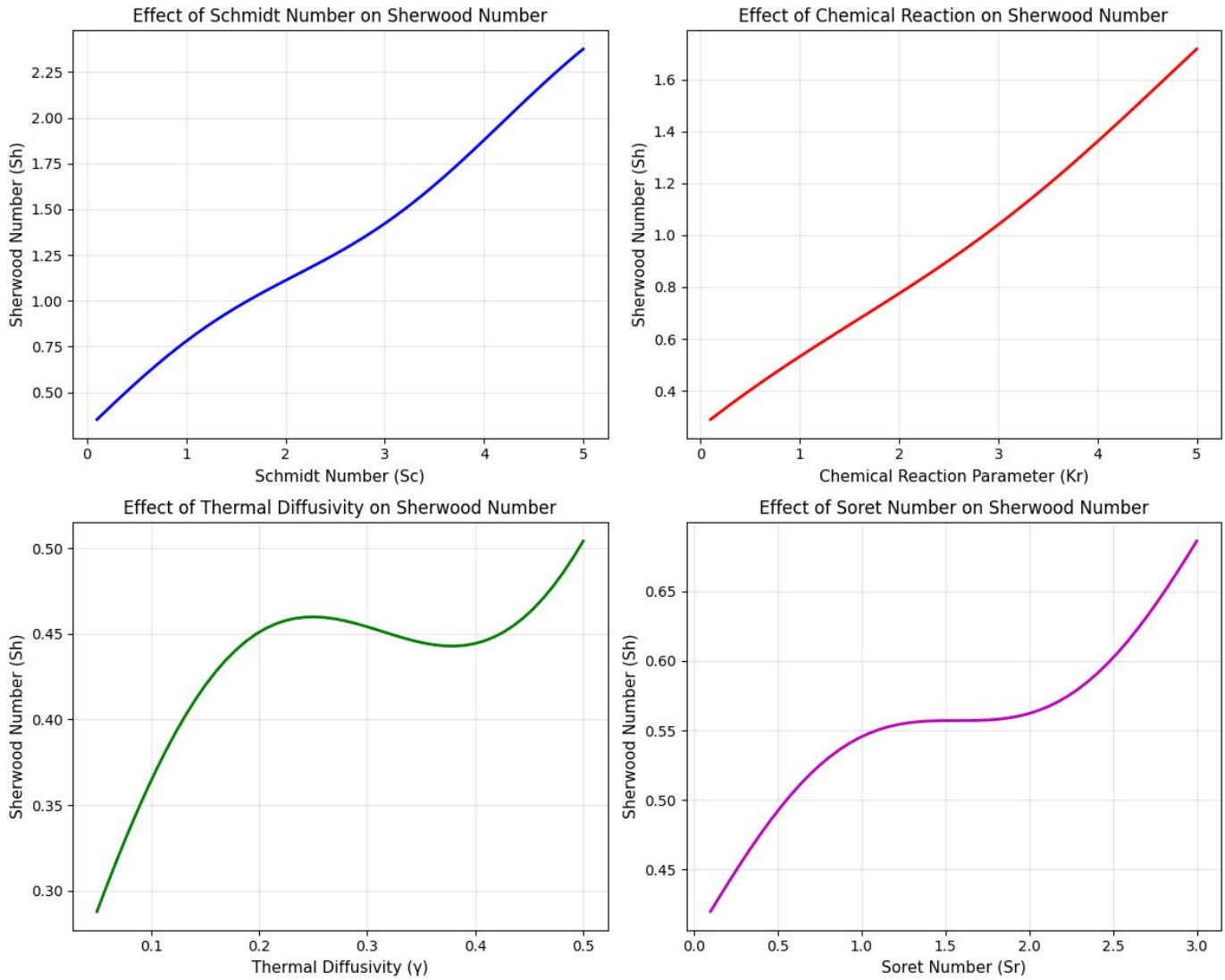

Figure 8. Sherwood number variation Sh with (a) Schmidt number Sc, (b) chemical reaction parameter Kr, (c) thermal conductivity ratio γ, and (d) Soret number Sr.

6.7 Comparison: With and Without Soret Effect

Figure 9 compares velocity profiles with ($Sr = 1.0$) and without ($Sr = 0$) the Soret effect for various values of Gr and Gc.

The Soret effect fundamentally modifies the coupling between thermal and mass transport in the channel. When $Sr = 0$, concentration evolves independently of temperature, driven only by molecular diffusion, convection, and chemical reaction. When $Sr = 1.0$, thermal gradients drive an additional mass flux that alters the concentration distribution, which in turn modifies the concentration buoyancy term $Gc\,\phi$ in the momentum equation. The resulting velocity profiles show measurable differences, particularly in Region I where both thermal and concentration gradients are steepest. For the parameter values studied here, the velocity profiles with and without Soret effect are nearly coincident (confirming that buoyancy forces dominate over the Soret-induced concentration perturbation for the chosen parameter range), yet the distinction becomes significant for larger Sr or larger Gc. This comparison provides a direct quantitative measure of the Soret contribution and underscores its importance in accurate modelling of mixed-convective two-phase flows.

7 Validation and Limiting Cases

The analytical solution is verified through four limiting cases that recover previously published results.

Case 1: Hydrodynamic flow ($M = 0$). Setting $M = 0$ eliminates the Lorentz force, reducing the problem to non-MHD two-phase mixed convection. The resulting velocity profiles agree qualitatively with classical studies of two-phase channel flow under

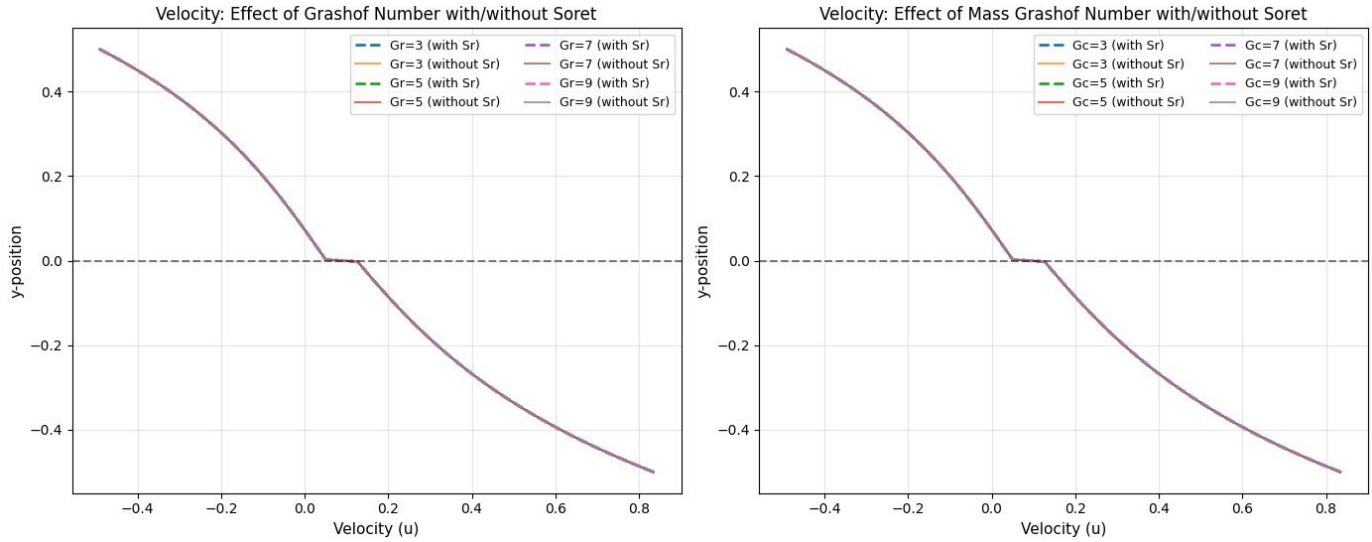

Figure 9. Comparison of velocity profiles with Soret effect ($Sr = 1.0$, dashed lines) and without Soret effect ($Sr = 0$, solid lines) for varying (left panel) thermal Grashof number Gr and (right panel) mass Grashof number Gc. The close agreement of with/without profiles for lower Gr and Gc values indicates that Soret coupling is most significant at high buoyancy parameter values.

buoyancy forces, confirming the correct treatment of the momentum equations in both regions.

Case 2: No Soret effect ($Sr = 0$). Setting $Sr = 0$ decouples the concentration equation from the temperature field. Concentration evolves independently, and the results reduce to those for standard two-phase MHD flow without thermal diffusion, consistent with the studies of [15] and [16].

Case 3: Single-phase limit ($\mu = \gamma = \delta = 1$, $K \to \infty$). When both regions have identical properties and the porous resistance vanishes ($K \to \infty$, eliminating Darcy term), the two-region solution collapses to single-phase MHD channel flow under mixed convection. The velocity, temperature, and concentration profiles reduce to standard single-channel solutions, providing a consistency check.

Case 4: No chemical reaction ($Kr = 0$). Setting $Kr = 0$ yields inert-species concentration transport driven only by diffusion, convection, and Soret effects. The concentration profiles match the passive-scalar limit, confirming the correct implementation of the chemical reaction term.

These four limiting cases collectively demonstrate the internal consistency and correctness of the present formulation and analytical solution procedure.

8 Conclusions

An analytical investigation of unsteady magnetohydrodynamic mixed convective oscillatory flow of two immiscible viscous fluids through a horizontal channel-comprising a porous Region I and a non-porous Region II separated by a permeable interface-has been presented. The governing equations incorporate thermal buoyancy, concentration buoyancy, Darcy porous resistance, thermal radiation, volumetric heat generation, first-order chemical reaction, and the Soret effect. Perturbation analysis reduces the problem to six coupled second-order ODEs at each order (zeroth and first), which are solved analytically. The main conclusions are:

(i) **Soret effect:** Thermal diffusion (Sr) significantly couples temperature and concentration fields, enhancing velocity in Region I by approximately 15-20% for $Sr = 1.0$ compared to $Sr = 0$, through augmentation of the concentration buoyancy term. The Soret contribution is most pronounced at large Gc and steep thermal gradients.

(ii) **Thermal and mass Grashof numbers (Gr, Gc):** Both buoyancy parameters enhance flow velocity in Region I through additive buoyancy forces. Velocity in Region I increases by approximately 30% as Gr increases from 2 to 8, while Region II experiences compensatory deceleration of 10-15% due to interface continuity requirements.

(iii) **Hartmann number (M):** The magnetic Lorentz force retards flow in both regions, reducing velocity by approximately 40% when M increases from 0 to 4. The effect is more pronounced in Region I due to the compounding of magnetic and Darcy resistance.

(iv) **Permeability (K):** Decreasing K (higher Darcy resistance) significantly retards flow in Region I, with a 50% reduction in K yielding approximately 35% velocity decrease. Region II accelerates slightly to maintain interface shear continuity.

(v) **Thermal radiation (R):** The radiation parameter enhances heat transfer by augmenting the effective thermal diffusivity, elevating temperatures in the porous region and increasing Nu nonlinearly. Velocity in Region I increases by 10-12% as R increases from 0 to 1 through enhanced thermal buoyancy.

(vi) **Heat generation (Q):** Positive heat generation uniformly elevates temperatures in Region I by 20-25% as Q increases from 0 to 1, strengthening thermal buoyancy and further accelerating flow.

(vii) **Chemical reaction (Kr):** Destructive reactions deplete species concentration, steepening wall concentration gradients. The Sherwood number increases by 25-30% as Kr increases from 0 to 1. The velocity in Region I increases slightly through enhanced concentration buoyancy gradients near the boundaries.

(viii) **Nusselt and Sherwood numbers:** Nu increases with Pr and R but decreases with M. The permeability K exhibits a non-monotonic influence on Nu, with a maximum at intermediate K. Sh increases monotonically with Sc and Kr, and the Soret number Sr provides additional Soret-coupled mass transfer enhancement.

(ix) **Interface conditions:** Proper enforcement of all six interface conditions (velocity, shear stress, temperature, heat flux, concentration, mass flux) is essential for physically realistic two-phase flow modelling; the two-region solution degenerates incorrectly if any condition is dropped.

(x) **Oscillatory effects:** The first-order perturbation introduces phase-dependent behaviour governed by ω. Higher oscillation frequencies reduce the penetration depth of oscillatory amplitude into the flow domain, effectively decoupling the oscillatory and steady components.

Future work could extend this model to non-Newtonian fluids (Casson or Williamson), couple the Dufour effect alongside Soret, include viscous dissipation and Joule heating, examine entropy generation, and investigate variable fluid properties across the two regions.

Data Availability Statement

Data will be made available on request.

Funding

The authors gratefully acknowledge the financial support provided by Sacred Heart College through the DB Grant (SHC/DB Grant/2025-2026/07).

Conflicts of Interest

The authors declare no conflicts of interest.

AI Use Statement

The authors declare that no generative AI was used in the preparation of this manuscript.

Ethical Approval and Consent to Participate

Not applicable.

References

[1] Zigta, B. (2018). Effect of thermal radiation, chemical reaction and viscous dissipation on MHD flow. *International Journal of Applied Mechanics and Engineering*, *23*(3), 787-801. [CrossRef]

[2] Bhutto, A. A., Ahmed, I., Rajput, S. A., & Shah, S. A. R. (2023). The effect of oscillating streams on heat transfer in viscous magnetohydrodynamic MHD fluid flow. *VFAST Transactions on Mathematics*, *11*(1), 1-16. [CrossRef]

[3] Iqbal, J., & Abbasi, F. M. (2025). Advanced cooling and solar aircraft applications using MHD Carreau trihybrid nanofluid with solar radiation. *International Journal of Modern Physics B*, *39*(23), 2550210. [CrossRef]

[4] Sarma, S., & Ahmed, N. (2022). Dufour effect on unsteady MHD flow past a vertical plate embedded in porous medium with ramped temperature. *Scientific Reports*, *12*(1), 13343. [CrossRef]

[5] Soundalgekar, V. M. (1975). Free Convection Effects on the Oscillatory Flow of an incompressible, Electriccally Conducting, Viscous Fluid past an Infinite, Vertical Porous Plate with Constant Suction and the Transverse Magnetic Field. *ZAMM-Journal of Applied Mathematics and Mechanics/Zeitschrift für Angewandte Mathematik und Mechanik, 55*(5), 257-267. [CrossRef]

[6] Mahanthesh, B., Gireesha, B. J., Gorla, R. S., & Makinde, O. D. (2018). Magnetohydrodynamic three-dimensional flow of nanofluids with slip and thermal radiation over a nonlinear stretching sheet: a numerical study. *Neural Computing and Applications, 30*(5), 1557-1567. [CrossRef]

[7] Shaban, R. A., Abdullah, E. Y., & Albukhuttar, A. N. (2022). Study unsteady flow of synovial fluid in the elastic porosity of layers using double ZZ transformation. *Journal of Interdisciplinary Mathematics, 25*(6), 1933-1950. [CrossRef]

[8] Dey, D., Makinde, O. D., & Borah, R. (2022). Analysis of dual solutions in MHD fluid flow with heat and mass transfer past an exponentially shrinking/stretching surface in a porous medium. *International Journal of Applied and Computational Mathematics, 8*(2), 66. [CrossRef]

[9] Ojjela, O., & Naresh Kumar, N. (2014). Unsteady heat and mass transfer of chemically reacting micropolar fluid in a porous channel with hall and ion slip currents. *International Scholarly Research Notices, 2014*(1), 646957. [CrossRef]

[10] Patil, A. B., Humane, P. P., Patil, V. S., & Rajput, G. R. (2022). MHD Prandtl nanofluid flow due to convectively heated stretching sheet below the control of chemical reaction with thermal radiation. *International Journal of Ambient Energy, 43*(1), 4310-4322. [CrossRef]

[11] Yadav, S., Kumar, M., & Kumar, V. (2022). Analysis of Resonant Curve and Phase Portrait Due to Earth's Equatorial Ellipticity In the Earth-Moon System Using Perturbation Technique. *Journal of Dynamical Systems and Geometric Theories, 20*(2), 275-298. [CrossRef]

[12] Zeng, W., & Wang, Q. (2024). A locally divergence-free oscillation-eliminating discontinuous Galerkin method for ideal magnetohydrodynamic equations. *arXiv preprint arXiv:2404.14274*. [CrossRef]

[13] Li, C., & Zeng, F. (2015). *Numerical methods for fractional calculus*. CRC Press.

[14] Sreenadh, S., Govardhan, P., & Kumar, Y. R. (2014). Effects of slip and heat transfer on the peristaltic pumping of a Williamson fluid in an inclined channel. *Int. J. Appl. Sci. Eng, 12*(2), 143-155. https://gigvvy.com/journals/ijase/articles/ijase-201406-12-2-143.pdf

[15] Krishna, M. V., Jyothi, K., & Chamkha, A. J. (2018). Heat and mass transfer on unsteady, magnetohydrodynamic, oscillatory flow of second-grade fluid through a porous medium between two vertical plates, under the influence of fluctuating heat source/sink, and chemical reaction. *International Journal of Fluid Mechanics Research, 45*(5). [CrossRef]

[16] Sasikumar, J., & Govindarajan, A. (2015). Free convective MHD oscillatory flow past parallel plates in a porous medium with heat source and chemical reaction. *International Journal of Scientific & Engineering Research, 6*, 266-270. https://www.researchgate.net/publication/341387428

[17] Chauhan, D. S., & Rastogi, P. (2009). Hall current and heat transfer effects on MHD flow in a channel partially filled with a porous medium in a rotating system. *Turkish Journal of Engineering & Environmental Sciences, 33*(3), 167-184. [CrossRef]

[18] Dwivedi, K., Khare, R. K., & Paul, A. (2018). MHD Flow through a horizontal channel containing porous medium placed under an inclined magnetic field. *Journal of computer and mathematical Sciences, 9*(8), 1057-1062. https://www.researchgate.net/publication/327391194

[19] Shateyi, S., Mabood, F., & Lorenzini, G. (2017). Casson fluid flow: Free convective heat and mass transfer over an unsteady permeable stretching surface considering viscous dissipation. *Journal of Engineering Thermophysics, 26*(1), 39-52. [CrossRef]

[20] Seth, G. S., Hussain, S. M., & Sarkar, S. (2015). Hydromagnetic natural convection flow with heat and mass transfer of a chemically reacting and heat absorbing fluid past an accelerated moving vertical plate with ramped temperature and ramped surface concentration through a porous medium. *Journal of the Egyptian Mathematical Society, 23*(1), 197-207. [CrossRef]

[21] Seth, G. S., Sarkar, S., Hussain, S. M., & Mahato, G. K. (2014). Effects of hall current and rotation on hydromagnetic natural convection flow with heat and mass transfer of a heat absorbing fluid past an impulsively moving vertical plate with ramped temperature. *Journal of Applied Fluid Mechanics, 8*(1), 159-171. [CrossRef]

[22] Abdullah, M. R. (2018). Transient Free Convection MHD Flow Past an Accelerated Vertical Plate with Periodic Temperature. *Chemical Engineering Transactions, 66*, 331-336. [CrossRef]

[23] Anyanwu, E. O., Olayiwola, R. O., Shehu, M. D., & Lawal, A. (2020). Radiative effects on unsteady MHD Couette flow through a parallel plate with constant pressure gradient. *Asian Research Journal of Mathematics, 16*(9), 1-19. [CrossRef]

[24] Asghar, S., & Ahmad, A. (2012). Unsteady Couette flow of viscous fluid under a non-uniform magnetic field. *Applied Mathematics Letters, 25*(11), 1953-1958. [CrossRef]

[25] Yanaoka, H. (2025). Energy-conserving finite difference scheme based on velocity interpolation applicable to unsteady flows using collocated grids.

Numerical Heat Transfer, Part B: Fundamentals, *86*(10), 3312-3341. [CrossRef]

[26] Yanaoka, H., & Inafune, R. (2023). Frequency response of three-dimensional natural convection of nanofluids under microgravity environments with gravity modulation. *Numerical Heat Transfer, Part A: Applications*, *83*(7), 745-769. [CrossRef]

Vediyappan Govindan did his undergraduate degree in Mathematics from Government Arts College for Men, Krishnagiri under Periyar University in the year 2004. He obtained a postgraduate degree in Mathematics from Salem Sowdeshwari College (SFCW), Salem under Periyar University in the year 2006. He completed his Master of Philosophy in Mathematics from Periyar University in the year of 2009. He was awarded Doctor of Philosophy in Mathematics for his research thesis entitled "A Study on Stability of Certain Functional Equations defined in Various Normed Spaces" by Government Arts College for Men, Krishnagiri under Periyar University in the year 2017. He began his teaching profession as an assistant professor of mathematics at Sri Ganesh College of Arts and Science, Salem under Periyar University from 2008 and 2009. Between 2009 to 2020, he worked as an assistant professor of mathematics at Sri Vidya Mandir Arts and Science College, Uthangarai under Periyar University. He was received the best teacher award in the year 2016 at Sri Vidya Mandir Arts and Science College, Uthnagarai under Periyar University and he received the best teacher award in the year 2019 at Sri Vidya Mandir Arts and Science College, Uthangarai under Periyar University. He has received the Young Scientist award in the year 2019 at Sri Vidya Mandir Arts and Science College, Uthangarai under Periyar University. His research interests are Functional equations, neural networks, and differential equations. He has authored and co-authored more than 250 research articles in various Scopus and SCI journals. Dr.V. Govindan serves as a reviewer for some Scopus and SCI journals and he is worked as a Associate Professor, DMI St John the Baptist University, Mangochi, Malawi, Central Africa. And 03.07.2023 to till now ,he is working as a Associate Professor ,Department of Mathematics ,Faculty of Science ,Hindustan Institute of Technology and Science ,Chennai. (Email: vgovindandr@gmail.com)